Lithium Conductivity and Ions Dynamics in LiBH$_4$/SiO$_2$ Solid-Electrolytes Studied by Solid-State NMR and Quasi Elastic Neutron Scattering and Applied in Lithium-Sulfur Batteries.

Jessica Lefevr[1], Luca Cervini[2], John M. Griffin[2], Didier Blanchard[1*]

[1] Department of Energy Conversion and Storage, Technical University of Denmark,

Frederiksborgvej 399, DK-4000 Roskilde, Denmark.

[2] Department of Chemistry, Lancaster University, Lancaster LA1 4YB, United Kingdom

[*] corresponding author Tel: +45 46775818, email: dibl@dtu.dk

Abstract

Composite solid-state electrolytes based on ball-milled $LiBH_4/SiO_2$ aerogel exhibit high lithium conductivities and we have found an optimal weight ratio, 30/70 wt% $LiBH4/SiO_2$, with a conductivity of 0.1 mS/cm^{-1} at room temperature. We have studied the Li^+ and BH_4^- dynamics using Quasi- Elastic Neutron Scattering and solid-state Nuclear Magnetic Resonance and found that only a small fraction (~10%) of the ions have high mobilities while most of the $LiBH_4$ shows behavior similar to macrocrystalline material. The modified $LiBH_4$ is formed from interaction with the SiO_2 surface and most probably from reaction with the surface silanol groups. We successfully applied these composite electrolytes in lithium-sulfur solid-state batteries. The batteries show reasonable capacity retention (794 mAhg^{-1} sulfur after 10 discharge-charge cycles, coulombic efficiency of 88.8% $\pm$ 2.7% and average capacity loss of 7.2% during the first 10 cycles).

1. INTRODUCTION

During the last two decades, lithium-ion batteries have become a common type of rechargeable batteries due to their higher energy densities than lead-acid, nickel–metal hydride and nickel-cadmium batteries.[1] Growing energy demands require further increase in electricity storage capacities however this is difficult to achieve with the current Li-ion technologies as, despite large research efforts, only marginal improvements in the capacities of the electrodes materials are expected. Instead, new battery chemistries have to be developed and lithium-air and lithium-sulfur (Li-S) are some of the most promising, offering very high theoretical energy densities.[2,3]

Lithium-sulfur batteries are forecasted as next generation batteries for mobile and automotive applications due to their high gravimetric energy density (1675 $mAhg^{-1}$ sulfur at 2.15 V),[4–10] up to 5 times higher than the theoretical capacities of the state-of-the-art lithium-ion batteries, such as lithium iron phosphate ("LFP", 170 $mAhg^{-1}$ at 3.4 V),[10] lithium ion manganese oxide ("LMO", 148 $mAhg^{-1}$ at 4.1V)[11] and lithium nickel manganese cobalt oxide ("NMC", 170 $mAhg^{-1}$ at 4.4 V).[10] Advantageously, and apart from this high theoretical capacity, Li-S batteries use sulfur in the positive electrode. Sulfur is one of the most abundant, and therefore cheap, elements in the earth's crust,[1] and furthermore it is benign and environmentally friendly. The overall electrochemical reaction in a Li-S battery can be written as:

$S_8 + 16Li \rightleftarrows 8Li_2S$; E_0= 2.15V vs Li/Li$^+$ Eq. 1

However some obstacles have to be overcome in order to make the technology commercially available. One of the major challenges with Li-S batteries is the solubility of the intermediate polysulfides (Li_2S_x, $4 \leq x \leq 8$) in liquid electrolytes, and the resulting shuttle between the negative electrode and positive electrode resulting in low Coulombic efficiency and fast self-discharge. [12,13] Various strategies have been employed to suppress the polysulfide shuttle. For example, surface modifications of the sulfur electrodes,[12,14,15] S encapsulation [16] or utilization of membranes to block

the polysulfides.[17] Each of these methods, while showing good improvements, is still at early stages of research and might induce large cost increases in the cell manufacturing. Therefore another strategy would be to replace the liquid electrolytes by fast ion-conducting solids.[18–23]

A number of different materials have been investigated as potential electrolytes for solid-state lithium batteries, including oxide and oxinitride glasses, such as LiPON,[24] LiGePS and LISICON.[25] LISICON and LiGePS compounds are good Li^+ conductors (10^{-2}-10^{-3} Scm^{-1} at room temperature)[26,27] but are unstable against Li metal and their stoichiometry is difficult to control during the synthesis.[27] Complex metal hydrides are also considered as possible electrolytes in solid-state batteries.[28,29] Lithium borohydride ($LiBH_4$) is a complex metal hydride, which has been widely studied as a solid-state hydrogen storage material [30–32] and more recently as an electrolyte for solid-state batteries.[33–37] $LiBH_4$ has two known polymorphs: a room temperature orthorhombic (*Pnm*a) phase with a low ionic conductivity and above 393 K a hexagonal phase (*P6₃mc*), with a high ionic conductivity (~1 mS.cm^{-1}).[38]

Stabilization of the hexagonal phase, at room temperature, is possible via the formation of solid solutions with lithium halides, such as LiI, LiBr and LiCl.[39–42] The solid solutions with LiI have high Li^+ conductivity (1 mScm^{-1} at 333 K) [34,39] and performances of the lithium borohydride / lithium halide solid solutions as solid electrolytes have been studied in Li-ion batteries.[41]

Confinement of $LiBH_4$ in mesoporous silica scaffolds has also been proved to give electrolyte of high Li^+ conductivity (0.1 mS.cm^{-1} at room temperature).[43] The confined composites are stable at least up to 6V and when cycled at elevated temperature (up to 413 K). The performances of nanoconfined lithium borohydride have been studied in lithium-sulfur batteries.[44] We have proposed that the fast lithium ionic conductivity originates from the existence of an interfacial layer between $LiBH_4$ and the SiO_2 walls of the mesoporous scaffolds [43] and following these results, Choi et al.,[45] have investigated ball milled composites made of $LiBH_4$ and two types of SiO_2: MCM-41

and fumed silica and more recently studied $LiBH_4/Al_2O_3$ composites [46] and reported conductivities comparable to the one we measured for nanoconfined $LiBH_4$ in MCM-41. They also proposed, however without any direct method of investigations but using a percolation model that the high Li^+ conductivity originates from the $LiBH_4/SiO_2$ interfacial layers formed during ball milling. One advantage of the synthesis method of Choi et al. is its simplicity. Indeed, nanoconfinement via melt infiltration requires high hydrogen pressure (up to 100 bar H_2 during heating) [43] and high temperature (568 K), while ball milling can be performed, under inert atmosphere, at ambient pressure and temperature.

In this paper we confirm and further investigate the origins of the high Li^+ conductivity in composite solid electrolytes synthesized by ball milling $LiBH_4$ and silica aerogel. We performed a detailed study on the ions mobility in the solid electrolyte using Quasi-Elastic Neutron Scattering (QENS) and Nuclear Magnetic Resonance (NMR) measurements. The results compare to the ones obtained for nanoconfined $LiBH_4$ in different scaffolds and as a new fact for ball milled $LiBH_4/SiO_2$ prove that not only the lithium mobility is increased but also that of BH_4^-. This suggests that confinement effects like size reduction of the crystallites, induced strain etc., are not the most important to obtain high Li^+ conductivity, but rather that the interaction at the interfacial layer, between the ionic salt and SiO_2 via the reaction of BH_4^- with the surface SiO_2 silanol groups, is the key parameter. Thereafter, we demonstrate the possibility to build solid-state batteries around this composite electrolyte through successful cycling of lithium sulfur batteries at 328 K (55ºC), reaching high energy densities, high degree of utilization of the sulfur and high coulombic efficiencies.

2. EXPERIMENTAL METHODS

Preparation of Electrodes

For all electrochemical measurements, the negative electrodes were prepared using lithium foil (Sigma Aldrich, 99.9%, thickness 40 µm). The positive electrodes were prepared from sulfur and carbon composites as described by Das, et al[44] combining ball milling and melt-diffusion of S. Ketjen Black EC-600JD (total surface area 1400 m^2/g with pore volume of 4.80-5.10 m^3/g, Shanghai Tengmin Industry Co. Ltd.) and activated carbon Maxsorb MCS-30 (surface area 3000 m^2/g, Maxsorb, Japan) were mixed in weight ratio 1:1. Elemental sulfur (Sigma Aldrich, 99.9%) was mixed with the carbon blend (S:C weight ratio 45:55) by ball milling for 30 min (400 rpm, BRP 125:1) using a Fritsch Pulverisette P7 planetary ball mill. Tungsten carbide balls and stainless steel vials were used. After ball milling, the mixture was heated for 6 hours at 428 K with slow heating and cooling rates (0.2 K/min.) in a sealed vessel with Ar atmosphere. When the C/S composite cooled to room temperature, it was mixed with 15% polyvinylidene fluoride (PVDF) and the resulting mixture was dispersed in N-methylpyrrolidinone (NMP) and left for stirring overnight. The resulting slurry was tap casted on 0.2 mm thick aluminum foil and dried at 55˚ C for 24 hours. After that the foil with casted C/S composites was punched out as disks of 10 mm in diameter (resulting thickness of C/S layer 15 µm evaluated from FIB-SEM micrographs). The thickness of the electrode is small and there is no need to incorporate lithium ion conducting phase. Good interface and contact is established between the electrode and the electrolyte when pressing the cell during its assembly; this was proven by the charge/discharge cycling of the tested cells both herein and in reference [44] in which the same methodology was used.

Preparation of Solid Electrolyte

The solid electrolyte was prepared using $LiBH_4$ powder (95% purity – Alfa Aesar) and SiO_2 aerogel (99% purity – Sigma Aldrich) which was dried prior usage at 393 K for 12 hours in a vacuum oven

(Büchi, Switzerland). Mixtures of the two components were ball milled using a Fritsch Pulverisette P7 rotating at 500 rpm for 5 hours. 1.0 g of $LiBH_4$ /SiO_2 composites together with 5 tungsten carbide balls were loaded in stainless steel vials under Ar atmosphere.

Batteries Assembly

The batteries were manufactured using specially developed cells described by Das, et al[44]. The cell assemblies were performed in a glovebox under Ar atmosphere and from the top of the piston in layers, starting with lithium discs cut with a diameter of 10 mm at the negative electrode side, followed by 65 mg of solid electrolyte and a disc with C/S composite on the positive electrode side. After assembling the cell was pressed with 1.5 ton.cm^{-2}.

Electrochemical Measurements

Once the batteries were assembled, they were placed into a climate chamber at 55°C, connected to a potentiostat (VMP3 - Bio-Logic SAS, France) and the Open Circuit Voltage (OCV) was measured for 1 hour. Thereafter, electrochemical impedance spectroscopy measurements (EIS) were performed before and after each charge/discharge cycle. EIS measurements were performed in the frequency range from 1 Hz to 1 MHz. The batteries were charged/discharged in the galvanostatic regime with current of 5 μA corresponding to a C-rate of 0.03 C based on the theoretical capacity of 1675 mAh.g^{-1} sulfur. The cutoff voltages were 1.0 V for discharge and 3.5 V for charge.

EIS measurements were also performed on composites $LiBH_4$/SiO_2 of different weight ratio in order to obtain the electrolyte with the best conductivity. EIS were measured by alternating current (AC) impedance spectroscopy using a PARSTAT 2273 potentiostat. The composite electrolytes were pressed into pellets of diameter 13 mm and thickness of ~1 mm in between two lithium foils (Sigma Aldrich Co., purity 99.9%) serving as non-blocking electrodes. A pressure of 1 ton/cm^2 was used, giving a final porosity estimated to be around 0.3 to 0.4. All preparation and measurements were carried out under Ar atmosphere. The frequency range of the AC impedance measurements was set

from 100 mHz to 1 MHz. The pellets were cycled in temperature from 303 K to 413 K. Before each measurement point, a 60 minutes dwell time was used for the pellet temperature to equilibrate.

Nuclear Magnetic Resonance Measurements

The magic angle spinning nuclear magnetic resonance (MAS-NMR) spectra were recorded using a Bruker Avance III spectrometer with a 16.4 T magnet and using a 2.5 mm probe with a MAS frequency of 15 kHz. MAS-NMR spectra were recorded using a ^{7}Li and ^{11}B pulse powers of 130 kHz and 100 kHz, respectively. Low power ^{1}H continuous wave decoupling was used, where the decoupling power was optimized for best spectral resolution. ^{1}H MAS-NMR spectra were recorded using the "Depth" pulse sequence[47] to minimize background signals associated with the probe and rotor components. In these experiments a ^{1}H pulse power of 110 kHz was used. The temperature in variable temperature experiments was calibrated using lead nitrate.[48]

Quasielastic Neutron Scattering

The Quasi-Elastic Neutron Scattering (QENS) measurements have been performed at IN16b, the backscattering spectrometer located at the Institut Laue-Langevin, Grenoble, France. We loaded 1 g of sample in aluminum flat cells of dimensions $30 \times 40 \times 0.5$ mm^3. The cells were oriented at 135° with respect to the direct beam. Si(111) monochromator and analyzer crystals were used in a back-scattering geometry, giving a final neutron wavelength of 6.271 Å and an energy resolution of 1 μeV. The QENS spectra were recorded by eighteen detectors corresponding to a scattering vector ranging from 0.50 to 1.96 Å^{-1} and at two different energy-transfer range ±5 and ±30 μeV. The spectra were analyzed by using the curve fitting utility (PAN) included in the DAVE package.[49] ^{7}Li and ^{11}B enriched LiBH$_4$ (purchased from Katchem) was used to avoid the strong neutron absorption from natural lithium and boron. Raw data available at http://dx.doi.org/10.5291/ILL-DATA.7-03-146.

3. Results and Discussions

LiBH$_4$/SiO$_2$ composites Li$^+$ conductivity

Electrochemical Impedance Spectroscopy (EIS) measurements performed on the composite electrolytes yield Nyquist plots consisting of single, slightly depressed semi-circles (See Figure S1 for a representative example). Although it suggests that only one process contributes to the ionic conduction, we cannot exclude that concurrent processes like bulk, grain boundary or conduction at the interface between LiBH$_4$ and SiO$_2$ exist but overlap in the Nyquist plots, as in this case it is not possible to separate these different contributions using only impedance spectroscopy.[50,51] The Nyquist plots are fitted using (*R-CPE*) equivalent circuit models, i.e. a resistor and a constant phase element in parallel. The intersection of the semicircle with the *Z'* axis in the low-frequency limit gives the pellet resistance, *R*, from which the electrolyte conductivity σ is calculated. **Figure 1** summarizes, with Arrhenius plots, the evolution with the temperature of the conductivities of composites with different stoichiometries.
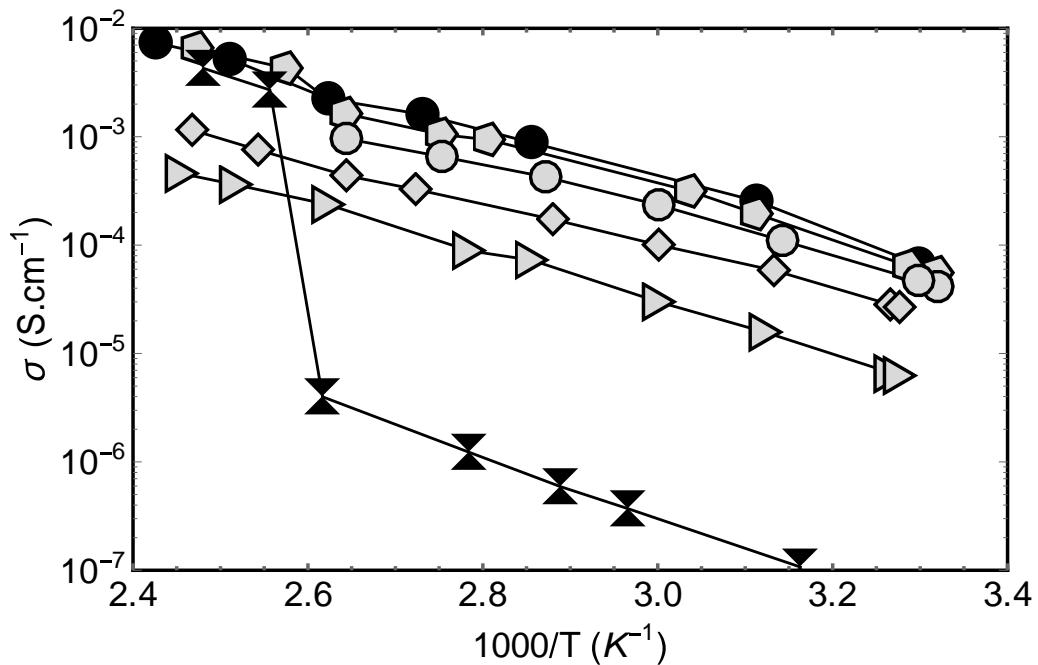
Figure 1. Arrhenius plots of the Li$^+$ conductivities obtained from EIS measurements on composites of different stoichiometry. Triangle (▷) 15/85wt% LiBH$_4$/SiO$_2$, diamond (◇) 25/75wt%, black

circles(●) 30/70 wt%, pentagons (⬠)40/60 wt%, gray circles(○) 50/50 wt%, black doubled triangles (✖) 90/10 wt%.

All stoichiometry exhibit enhanced conductivity when compared to the conductivity of LiBH₄, and the highest values, at any temperature below the phase transition of LiBH₄, are obtained for the 30/70wt% LiBH₄/SiO₂ composite (**Figure 2**). In a first approximation, the plots are considered as straight lines to extract apparent activation energies for the lithium conductivities however, for the larger LiBH₄ contents, jumps in the conductivity at the phase transition (383 K) exist and in that case only the points before the jumps are considered. The jumps in the conduction, at the temperature of the phase transition of LiBH₄, clearly illustrate that for lithium borohydrides rich composites, most of the LiBH₄ is not modified by the presence of SiO₂. For the middle range compositions the plot shows slight curvatures, ignored during the fitting, this is discussed in the text below, in the light of the NMR and QENS results. Choi et al. [45] have obtained similar results as the ones depicted in **Figure 1** and **Figure 2**.
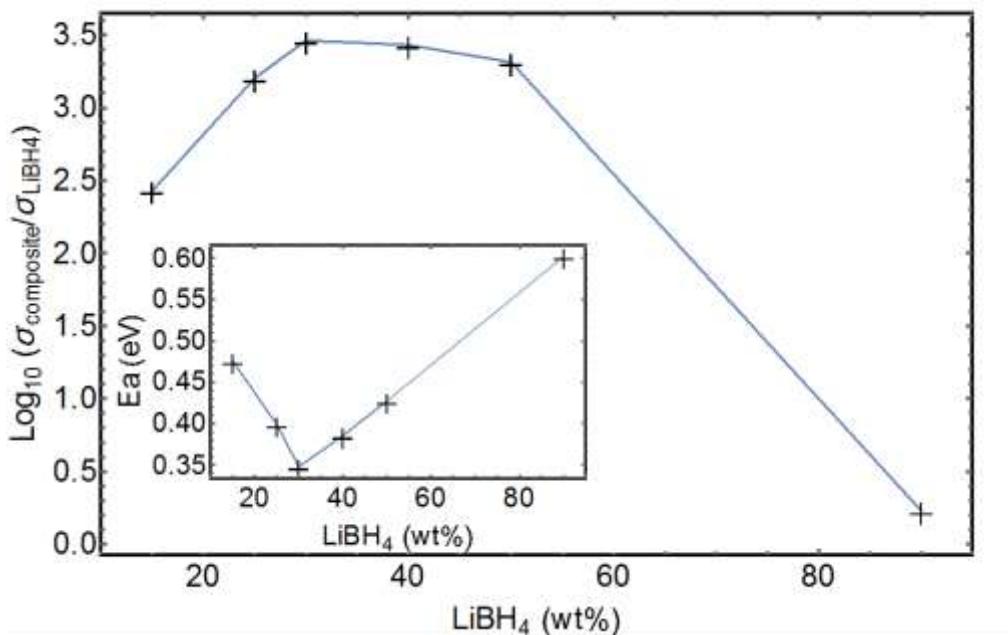
Figure 2. Logarithm of the conductivities at 303 K, normalized to the conductivity at 303 K of macrocrystalline LiBH₄, extracted from the Arrhenius plots of **Figure 1** for composites LiBH₄/SiO₂

of different stoichiometries. Insert: activation energies for Li$^+$ conduction extracted from the slopes of the Arrhenius plots of **Figure 1**.

They reported the highest conductivity (10^{-4} S·cm^{-1} at room temperature) for a composite with 55 vol.% of SiO$_2$ corresponding to our 30/70 wt% LiBH$_4$/SiO$_2$ ratio. We have obtained slightly lower conductivities, but also lower activation energies, ca. 0.35 eV for the 30/70wt% LiBH$_4$/SiO$_2$ composition compared to the 0.43 eV reported by Choi et al. for an equivalent LiBH$_4$/SiO$_2$ stoichiometry. The difference in the reported conductivities might be due to differences in the preparation of the composites and /or difference in the preparation of the pellets (pressure and method of preparation). It could also be due to the different silica used, presenting different particle sizes, surface areas and the presence of pores within the particles in the present study. The difference in the activation energy is not easy to understand.

Quasielastic Neutron Scattering
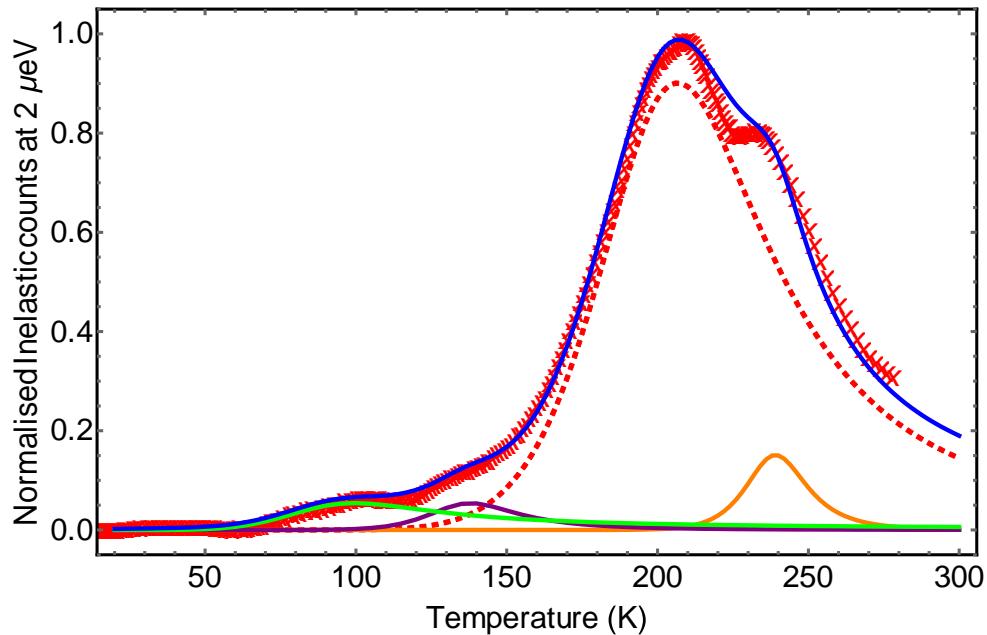
Figure 3. Normalized intensities at the energy transfer of ±2 μeV for 30/70 wt% $LiBH_4/SiO_2$ during heating from 3K to 280K. The red crosses are the experimental data, the blue line results from the fit using Eq.2 with four Lorentzian (green, purple, dashed red and orange lines).

In **Figure 3**, a plot of an inelastic fixed window scan (IFWS) is shown. It displays the sum over all accessible scattering vector, from 0.50 to 1.96 Å^{-1} of the intensities recorded at the energy transfer of ±2 μeV while the temperature was increased from 3 to 280 K. Similarly to IFWS measurements performed for unmodified $LiBH_4$,[52] the intensity increases to a maximum around 210 K and then decreases; however below that temperature two new local maxima are observed, at around 100 K and 140 K and above 210 K, the shoulder on the right of the main peak is better resolved. The better resolution of the shoulder compared to the published data[52] could be due to different experimental conditions, heating ramp, amount of sample into the neutron beam or to the sample itself.

Because the incoherent scattering cross section of hydrogen is much larger (80 barns) than that of any other of the composing atoms (^7Li: 0.78, ^{11}B: 0.22, Si: 0.015, O: 0 barns), the recorded quasi-elastic signal must originate from the motion of the hydrogen atoms. Mobilities of the ions in borohydrides have been deeply studied with a special focus on Li^+ and BH_4^- mobilities in macrocrystalline or nanoconfined $LiBH_4$.[53–63] Reorientational mobilities such as rotation about the 2-fold and 3-fold BH_4^- tetrahedral symmetry axes, tetrahedral tumbling and combination of those have been studied and documented using QENS. Confined $LiBH_4$ in nanoporous materials has been found to display at least two quasielastic components attributed to slowly and fastly reorienting anions. The more slowly reorienting anions have been associated with a macrocrystalline-like type $LiBH_4$, located outside or in the center of the pores while the more rapidly reorienting anions, to $LiBH_4$ located close to the pore surfaces.[64–66] In **Figure 3**, one can distinguish four quasielastic signals; two of lower intensity below 160 K and two of larger intensity above this temperature. The first two maxima can reasonably be attributed to species with the faster dynamics while the two last maxima can be attributed to anions behaving as in macrocrystalline $LiBH_4$. The observation of two

distinct dynamics in the low temperature orthorhombic phase of LiBH$_4$ has been reported in two NMR studies.[53,67] Two motions with different activation energies were observed and assumed to be due to rotations around the C$_2$ and C$_3$ axes of the BH$_4^-$ tetrahedron. Our measurements corroborate these findings (see text below) and together with the results published by Remhof et al.[52] are the first reports of such observation using QENS. In **Figure 3**, assuming that the observed quasielastic components would result in Lorentzian in the QENS spectra, as expected from BH$_4^-$ reorientational dynamics, the data have been fitted using the following expression:

$$I(T) = \sum_{n=1}^{4} 2 \times I_n \times L(2, \Gamma_n(T)) \qquad \text{Eq. 2}$$

where I_n are the respective scaling parameters of the four Lorentzian and $L(2, \Gamma_n(T))$ are their values at ±2 µeV. $\Gamma_n(T)$, the full widths at half maximum of the Lorentzian are assumed to follow Arrhenius behaviors as expected for thermally activated atomic motions i.e:

$$\Gamma_n(T) = \Gamma_{n,0} \times Exp(-\frac{E_n}{k_B.T}) \qquad \text{Eq. 3}$$

where E_n is the activation energy for the observed dynamics, k_B the Boltzmann constant.

In total 12 parameters were to fit and the starting graphically guessed values were set manually. A good fit was obtained with the values displayed in **Table 1**.

Table 1. Obtained values for the fitting parameters of the ±2 µeV temperature scan (**Figure 3**) using Eq. 2 and 3. Last column: activation energy from fits of the Arrhenius plot in **Figure 6**.

	I_n (a.u.)	$\Gamma_{n,0}$ (µeV)	E_n (eV)	E_a (eV)
L_1	6.8×10^{-7}	300	0.037	0.041
L_2	6.8×10^{-7}	160×10^3	0.126	0.14

L_3	1.13×10^{-5}	13×10^3	0.144	0.15
L_4	1.9×10^{-6}	2×10^5	0.55	-

QENS spectra were also collected in the temperature range from 3K to 290K and at two different energy-transfer windows ±5 and ±30 μeV. As expected from the IFWS, they consist of one elastic and one or two quasielastic components. The simultaneous, two quasielastic, components were seen only in the spectra taken with the ±30 μeV energy window. The elastic component comes from the incoherent scattering process with no detectable energy transfer while the quasielastic components reflect the energy transfer, either a gain or loss due to the hydrogen dynamics. **Figure 4** displays some chosen QENS spectra recorded with the energy transfer windows of ±5 μeV. Clear increasing Lorentzian broadenings accompanied by loss of the elastic intensities, are visible when the temperature increases. A similar plot can be found in the supplementary information for the QENS spectra collected with the energy transfer windows set to ±30 μeV (Figure S2). It is noteworthy that in the elastic line, the contribution from the silica as to be taken into account as it participates to ~10% of the signal intensity.
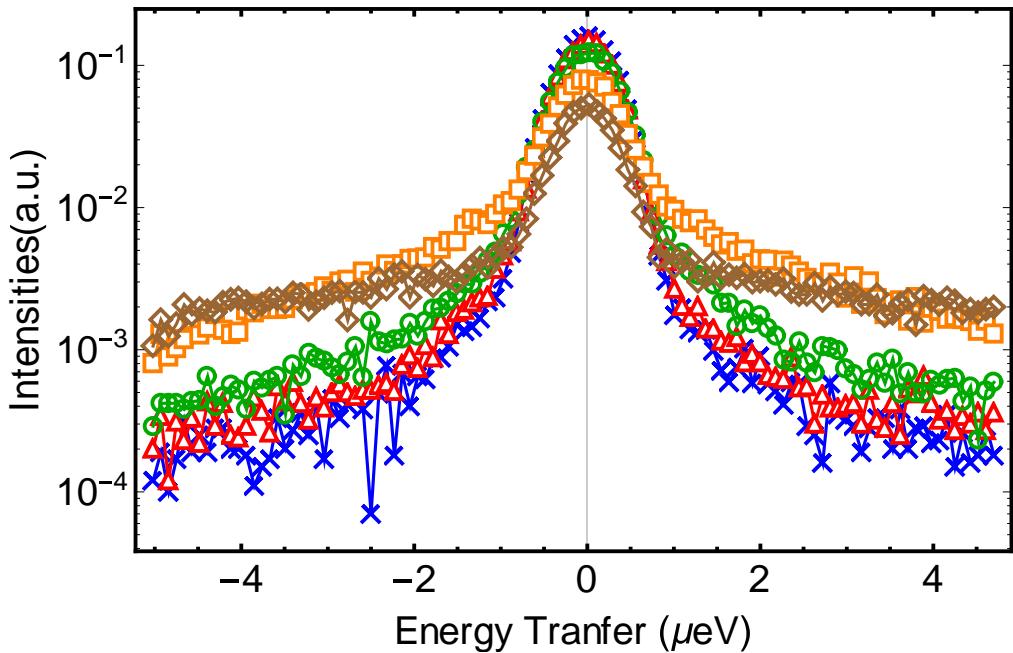
Figure 4. QENS Spectra for 30/70wt% LiBH4/SiO2, at Q=1.7239 Å^{-1} with a set energy transfer window of ±5 µeV and at, blue crosses: 80 K, Red triangles: 130 K, Green circles: 160 K, orange squares:200 K, Brown diamonds: 250 K.
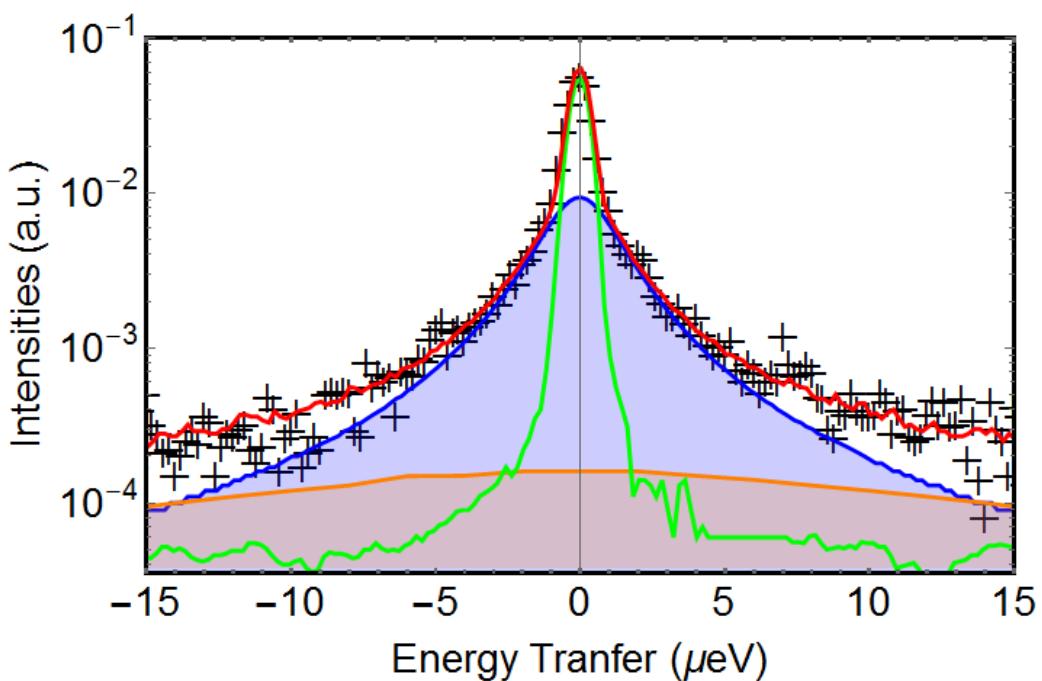
Figure 5. Fitted QENS spectrum for 30/70wt% LiBH$_4$/SiO$_2$, at Q=1.8466 Å^{-1} with a set energy transfer window of ±30 µeV. Black crosses: experimental data, green curve: resolution function (QENS at 3K), blue curve: first Lorentzian, orange curve: second Lorentzian.
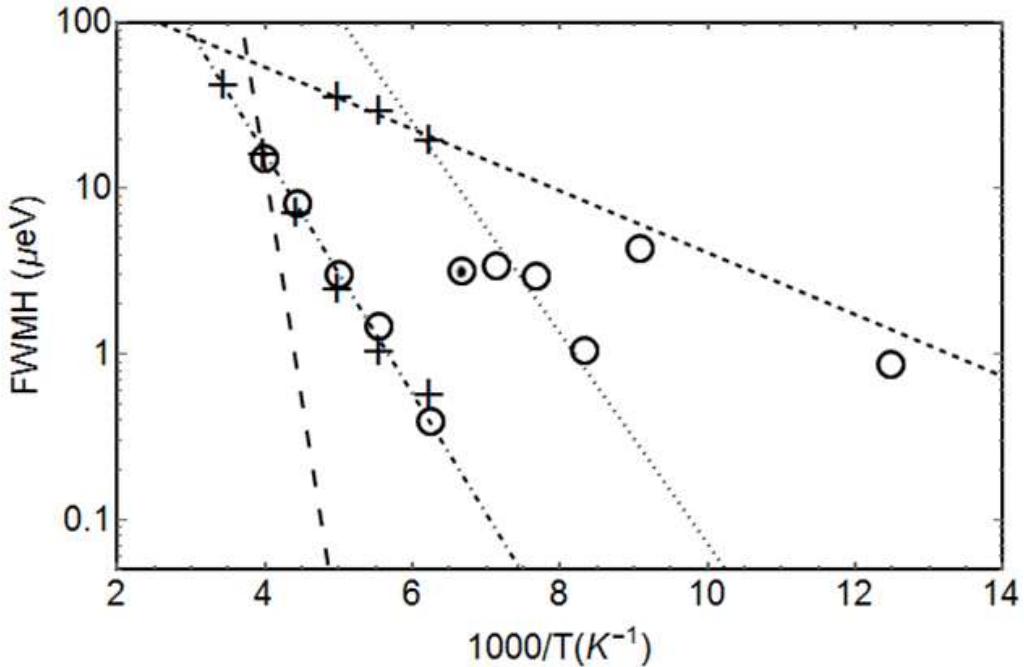
Figure 6. Arrhenius plots of the full width at half maximum of the QENS broadening. Crosses: from the spectra measured with the ±30 energy window, circles with the ±5 μeV energy window. The lines are the expected broadening obtained from the fit performed on the temperature scan (IFWS) displayed in **Figure 3** and using the parameters presented in **Table 1**

The **Figure 5** exemplifies a fit with two Lorentzian for a spectrum taken at 160K, energy window of ±30 μeV and Q=1.481 Å^{-1}.

The **Figure 6** presents Arrhenius plots of the full width at half maximum (FWHM) of the quasielastic broadenings. The value, for a given temperature, is the average of the values obtained for all the detectors. Indeed the values were found to be Q-independent, as expected for localized dynamics (See Figure S3-S5 for the detailed values). They were obtained after the fits of the QENS spectra at different temperatures and for the two different energy transfer windows (±5 and ±30 μeV). For the low temperature spectra (80K to 140K and ±5μeV), the fits at low Q values (Q<0.7 Å^{-1}) were not reliable since only a small fraction of hydrogen atoms appears mobile within the time resolution of IN16B, giving only a negligible quasielastic contribution. Therefore, the FWHM values were extracted for Q>0.7 Å^{-1} only. In the middle range temperature (130 < T < 150 K), the spectra were the most difficult to fit. In this temperature range there is an overlap of at least two

quasielastic broadenings and for example the dotted circle point seems to fall out of the series probably because the fit captured an average value between two quasielastic components. The lines on **Figure 6** represent the expected values of the Lorentzian FWHM calculated from the fits of IFWS (**Figure 3** and **Table 1**). One should note here the very good agreement between the Lorentzian widths obtained via the two approaches. It illustrates the importance to develop linear motor Doppler drives to perform such IFWS.[68] In **Table 1**, the Activation energies extracted from the Arrhenius plots are also shown (the actual fitting lines are not shown in **Figure 6** for clarity). The dotted circle was removed from the fits, otherwise all other points were kept and the three activation energies obtained are similar to the ones obtained from the fit of the temperature scan for L1, L2 and L3. L4 is not visible in the QENS spectra as it would give either a narrow component, included in the elastic line, or a broad component overlapping with L1 or L3.

Due to their relative intensities in the QENS spectra (see text below about Elastic Incoherent Structure Factor) and IFWS, it is reasonable to attribute the dynamics observed with L1 and L2 to a small fraction of the total hydrogen atoms present in the composite, while L3 and L4 can be ascribed to the C_2 and C_3 reorientation of a larger fraction with slower dynamics and resembling macrocrystalline $LiBH_4$. Indeed, the activation energy for L3 corresponds typically to the values for bulk $LiBH_4$ in composite materials.[64,65] The activation energy values obtained for L1 and L2 are respectively smaller and larger than the published values obtained for nanoconfined $LiBH_4$ and attributed to fast reorientation of BH_4^-.[64,65] The dynamics observed were interpreted as isotropic rotational diffusion through a, combination of rotations, as found in the high temperature hexagonal polymorph of $LiBH_4$.[65] These published activation energies could represent an average of the values obtained herein for L1 and L2 and thus L1 and L2 would then be attributed to the C_2 and C_3 rotations of BH_4^-.

Another possibility could be that L1 and L2 correspond to two different species dynamics, BH_4^- as expected, but also BH_3 (See text below on the possible existence of BH_3). In such a case BH_4^- could follow C2, C3 or isotropic diffusion resulting in L1 or L2, while BH_3 would follow C_3 rotation.
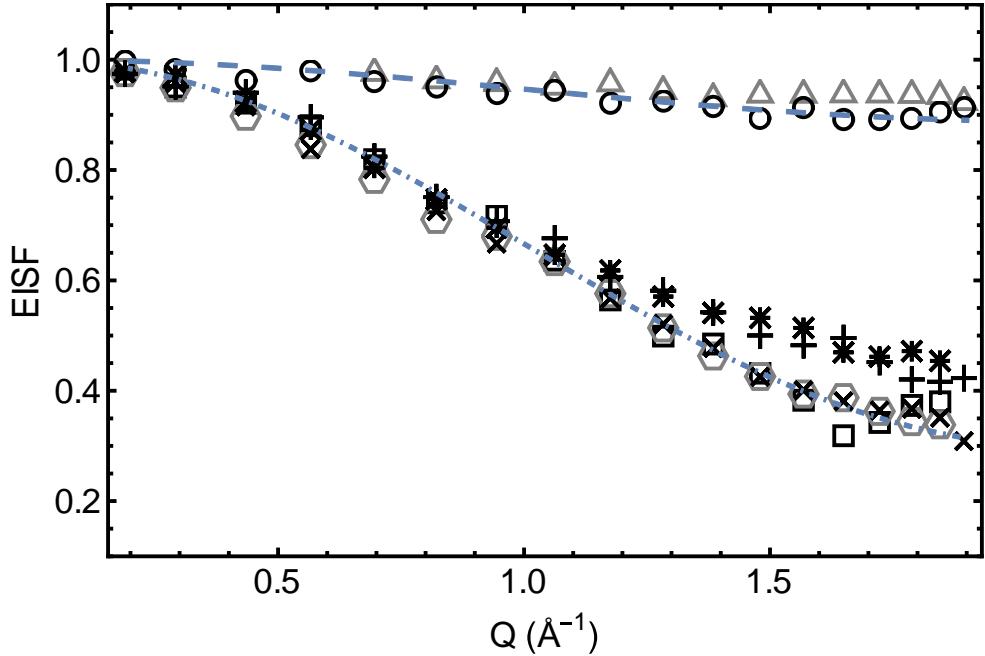
Figure 7. EISF of 30/70wt% $LiBH_4/SiO_2$ at selected temperatures. Open symbols, from the fits of the QENS spectra obtained with the± 5 μeV energy window (triangles: 140, circles: 150, squares 225, hexagons: 250 K). Other symbols from the fits of the QENS spectra obtained with the with the ± 30 μeV energy window (plus: 225, asterisks: 250K, X: 290K). The dashed lines represent models for the BH_4^- rotational diffusion, uniaxial jumps about the C_2 or C_3 axis (Equ.4). The upper line is for p=0.16, the lower line for p=1.

The elastic incoherent structure factor (EISF) is the fraction of the total quasielastic intensity contained in the purely elastic peak. It is a measurable quantity evaluated as function of Q from the ratio of the integrated elastic intensity over the total scattered intensities. It may reveal the geometry of the observed dynamics. The **Figure 7** displays some of the experimental EISFs, fitted with the models for C_2/C_3 hindered rotation as expressed in the following equation (the EISFs have the same expression for both rotation axis):

$$EISF = 1 - p + \tfrac{1}{2}p\left(1 + j_0\left(2\tfrac{\sqrt{2}}{\sqrt{3}}Qd\right)\right) \qquad \text{Eq. 4}$$

With j_0 the zeroth order Bessel function, d the B-H bond length and p the fraction of BH_x (x=3 or 4) participating to the observed quasielastic signals.

Fits for isotropic rotational diffusion (Eq.5),[69] were also performed for the low temperature EISFs (T<150 K), not apply for the higher temperatures as it would give EISFs values below 0.2 for Q>1.5 Å^{-1}and such low values have never been observed for LiBH$_4$ in the temperature range used in this study.

$$EISF = 1 - p + \tfrac{1}{2}p\left(1 + j_0\left(2\tfrac{\sqrt{2}}{\sqrt{3}}Qd\right)\right) \qquad \text{Eq. 5}$$

When the EISFs contain contribution from the more and less mobile species, the splitting of the elastic intensity is not known a priori and therefore we did not separate them and calculate global EISFs. Reasonable fits are obtained for the high temperature EISFs (T> 160K) with p=1 and d=1.21 Å the reported crystallographic B-H bond length in LiBH$_4$.[70] For the fit at lower temperature (T<150 K), keeping d=1.21 Å constant, different values of p were found ranging from 0.06 to 0.1, for the isotropic diffusion (Eq .5) and from 0.1 to 0.16 for C_2/C_3 (Eq.4) and increasing with temperature from 80 to 150K. It shows that the fraction of highly mobile species (BH$_4^-$ and/or BH$_3$) increases with temperature. However the obtained values suffer from rather large inaccuracies, mainly due to the difficulty to fit the QENS spectra with a low contribution from the quasielastic signal therefore, they should be considered as indicative only. In the temperature region where the contribution from the two populations are within the time resolution of IN16B, the EISFs deviate slightly from the model with p=1 as if the intensities of the quasielastic signal were underestimated. The origin for these deviations is not currently understood and needs further investigation.

NMR Measurements

Figure 8 shows single-pulse excitation spectra of ^7Li nuclei in 30/70wt% $LiBH_4/SiO_2$ electrolyte in the temperature range from 245 to 341 K. While for macrocrystalline $LiBH_4$, the spectrum comprises a single Lorentzian peak,[71] two peaks are observed for the composite. These two peaks can be fitted with Lorentzian functions as exemplified for the measurement performed at 341 K. The narrower component becomes even sharper with the increasing temperature (**Figure 8 -** right insert) as previously reported by Verkuijlen et al. for $LiBH_4$ nanoconfined in mesoporous silica.[71] The broad component with a shift similar to the one for macrocrystalline $LiBH_4$ is attributed to Li^+ motions in unmodified bulk-like $LiBH_4$, while the narrower component is attributed to more mobile Li^+ cations from some modification of $LiBH_4$. As reported by Verkuijlen et al., we observed no change in the relative intensities of the two components as function of temperature. (**Figure 8** - left insert). This is in opposition to the NMR results reported by Shane et al. [72] and QENS results from Verdal et al.[65] It is also in opposition to the QENS data reported herein but as already mentioned this might just illustrate the limited accuracy of the extraction of such quantities.
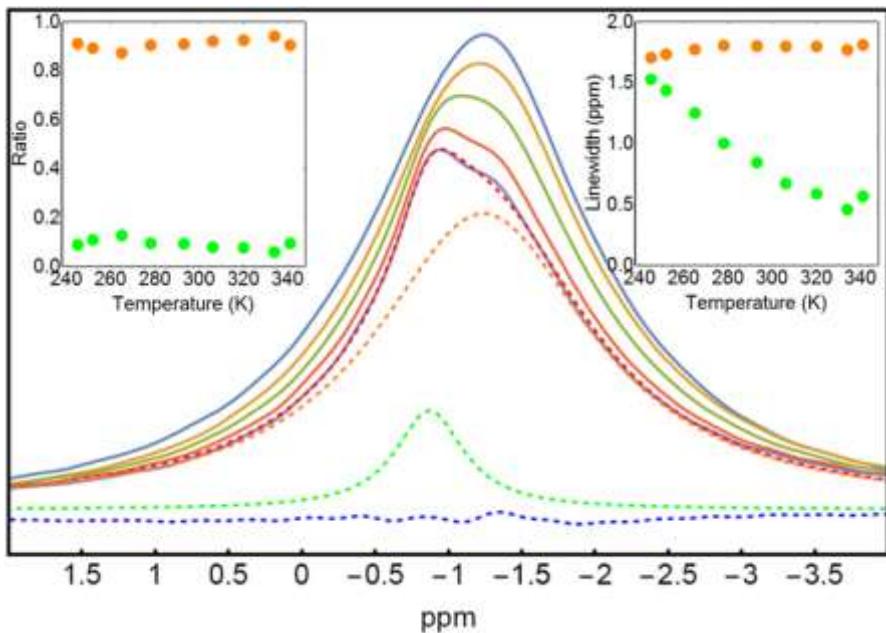
Figure 8. ^{7}Li single pulse excitation spectra for 30/70 wt% LiBH$_4$/SiO$_2$ without ^{1}H decoupling in temperature range from 245 to 341 K (top to bottom: 245, 265, 283, 320, 341 K). The orange and green dashed lines illustrate the fit (red dashed line) to spectrum recorded at 341 K – The blue dashed line shows the difference between fit and data. Left insert: relative intensities of two spectral components (orange: broad, green: narrow component). Right insert: line width of the two spectral components (orange: broad, green: narrow component).
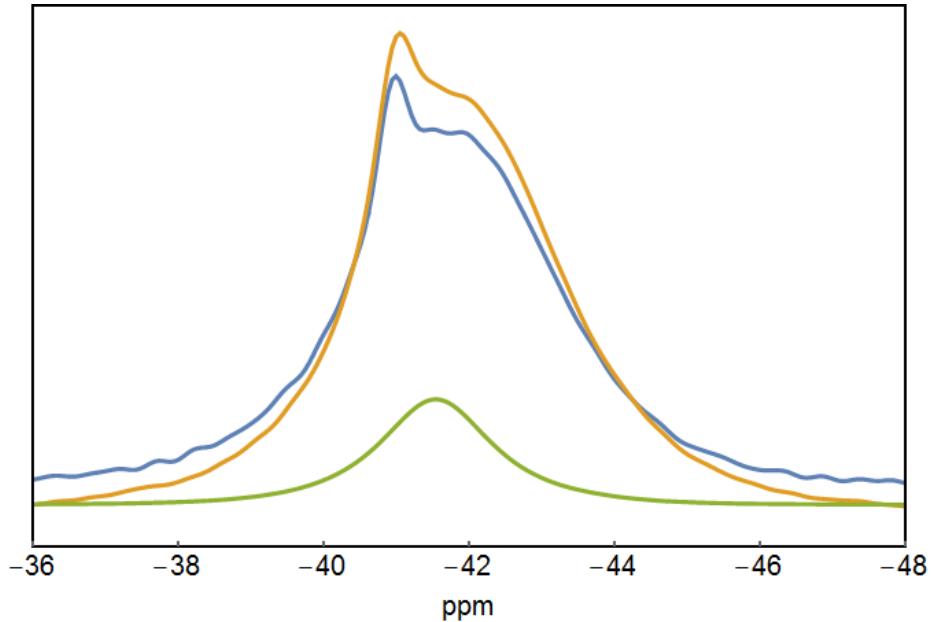
Figure 9. ^{11}B single pulse excitation spectra for pure LiBH$_4$ (green) and 30/70% wt% LiBH$_4$/SiO$_2$ at 294 K (blue) and 341 K (orange) with ^{1}H decoupling.

Figure 9 shows [11]B single pulse excitation spectra for pure LiBH$_4$ and 30/70% wt% LiBH$_4$/SiO$_2$ at 294 K and 341 K with ^{1}H decoupling. The [11]B resonance for the 30/70 wt% LiBH$_4$/SiO$_2$ composite is clearly different than for pure LiBH$_4$. At 341 K, two components are seen at -40.97 ppm and -41.93 ppm for the composite while the spectrum for LiBH$_4$ (at 294 K) shows a single resonance at -41.50 ppm. Hwang et al.[73] have observed the splitting of the central resonance in the [11]B spectrum for LiBH$_4$ in mesoporous silicates at temperatures above 373 K, i.e., when LiBH$_4$ is in the hexagonal crystal structure. Verkuijlen et al. [71] have also observed a similar splitting for the [11]B resonance, both with and without ^{1}H decoupling, for LiBH$_4$ nanoconfined in mesoporous silica but at lower temperatures, as low as 283 K. Their presented pattern without ^{1}H decoupling is similar to the one given by Shane at al.[74] for molten LiBH$_4$ at 558 K. Un- reported so far is the presence of a third components at -41.50 ppm observed herein at 294 K for the composite. It suggests that beside of the two different population of boron, with high and low mobilities, an intermediate one exists.
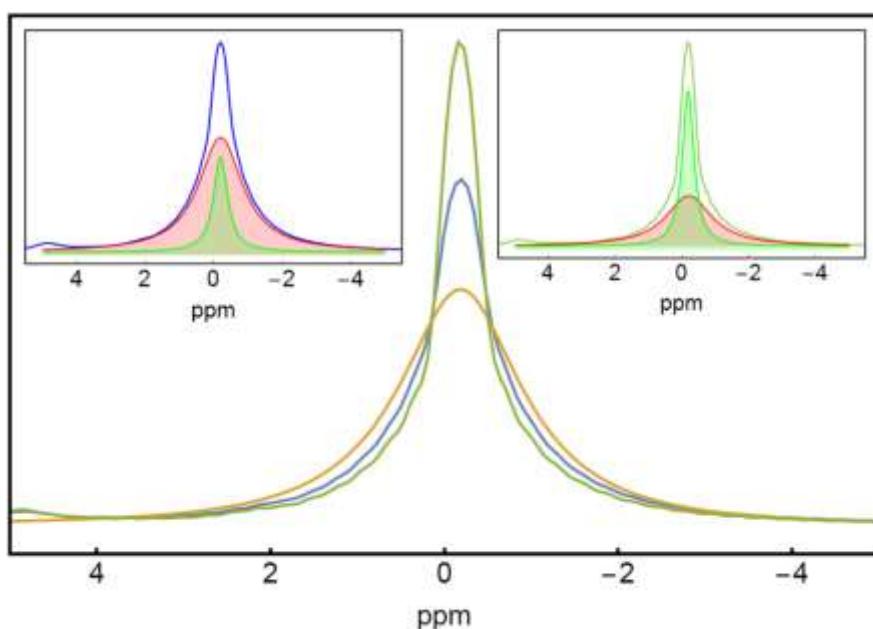
Figure 10. ^{1}H$^+$ single pulse excitation spectra for pure LiBH$_4$ (orange) and 30/70 wt% LiBH$_4$/SiO$_2$ at 294 K (blue) and 341 K (green). Inserts, left: 30/70 wt% LiBH$_4$/SiO$_2$ at 294 K and fit with two Lorentzian, right: at 341 K with two Lorentzian.

Figure 10 shows H$^+$ single pulse excitation spectra for pure LiBH$_4$ and 30/70 wt% LiBH$_4$/SiO$_2$ at 294 and 341 K. While the ^{1}H$^+$ spectrum for pure LiBH$_4$ shows a single peak at -0.2 ppm, the spectra for the composites show a superposition of a narrow central component and a broad component (See insert). This is similar to results from measurements reported by Verkuijlen et al. and Shane at al. who observed two components in the spectra for LiBH$_4$ in mesoporous silica or carbon aerogel, respectively.[71,72] They attributed the narrow component to more mobile hydrogen species than the one present in macrocrystalline LiBH$_4$ resulting in the broader component. This suggests that in 30/70 wt% LiBH$_4$/SiO$_2$, already at room temperature, a fraction of the H atoms move faster in the composite than in bulk LiBH$_4$. For the composite, a peak at 4.2 ppm is observed. Such a peak has been attributed to impurities[75] or to H$_2$ gas trapped inside of solid LiBH$_4$ as similar peak was observed in the case of H$_2$ trapped in AlH$_3$.[76] Hwang et al.,[73] performing NMR measurements while heating a mixture of LiBH$_4$ and SiO$_2$, observed this "H$_2$ peak" and proposed a reaction (Eq. 6) between the hydroxyl groups present at the surface of SiO$_2$ and LiBH$_4$, releasing hydrogen and occurring at about 373 K.

$$SiOH + [BH_4]^- \rightarrow SiO\text{-} BH_3 + H_2 \qquad\qquad\qquad Eq.\ 6$$

Hwang et al. also noticed the disappearance of the silanol peak (at 1.8 ppm), during heating of mixture of LiBH$_4$ and SiO$_2$. One can note that no peak is visible at 1.8 ppm in **Figure 10** for the composite spectrum. The existence of O-B bonds, supporting the existence of a reaction between the hydroxyl groups and LiBH$_4$, has been reported by Choi et al. [46] for LiBH$_4$ ball milled with

Al$_2$O$_3$. Catalytic activity of the hydroxyl group in forming mobile species for NaAlH$_4$ or NaH has also been reported,[77] and similar reaction can be expected for LiBH$_4$. In a recent work on LiBH$_4$:P$_2$S$_5$ systems, Unemoto et al [78] suggested, from QENS measurements, that BH species could form from BH$_4^-$ anions, not only as BH$_3$, but also BH$_2$ and possibly BH. The difference between mobility of BH$_4^-$ (seen as mobile) and BH$_2$ (seen as immobile) could explain the presence of the different populations in their QENS measurements. Explanation on the origin for these species was not given.

Herein, QENS and NMR measurements give strong evidences of the existence of a phase with highly mobile species (Li$^+$ and H), accounting for example to up to 10 (NMR) or 16% (QENS) of the LiBH$_4$ content in the 30/70 wt% composite at temperature below or close to room temperature. Undoubtedly this phase is at the origin of the high ionic lithium conductivity since the rest of the LiBH$_4$ is found to be, both from NMR and QENS but also from differential scanning calorimetry and X-Ray diffraction measurements (see Figures S8 and S9 in the supplementary information), in the low temperature crystal structure. The phase with highly mobile H/Li$^+$, might originate from the interfacial layer formed between LiBH$_4$ and SiO$_2$ as previously stated.[43] In agreement with Choi et al.,[45] we find an optimal LiBH$_4$/SiO$_2$ composition with an optimal conductivity as a result of the competition between increasing the fraction of the interfacial layer, i.e. increasing the surface area of SiO$_2$ by increasing its content and the necessity to have percolation network with a percolation threshold.

Heterogeneous doping has been known for long time as efficient and rather general solution to improve ionic transport in solids and the existence of space charge layers has been a common approach to explain the conductivity enhancement resulting from the dispersion of insulating phases into ionic conductors. See for example the work from Liang.[79] In the space charge layer model, at the interfacial layer, electroneutrality does not hold and large deviations of the ions concentration

might exist. LiBH$_4$ is a Frenkel disordered ionic crystal,[80] surface interactions between this ionic conductor and SiO$_2$ would stabilize or destabilize the mobile ions on the surface sites, increasing the concentration of charge carriers, vacancies or interstitials ions in the space charge region. Surface interactions might lead to SiO-BH$_3$ species, as depicted in Eq.6, and therefore contributes to increased conductivity of LiBH$_4$/SiO$_2$ composites. Choi et al. [46] report a larger density of B-O bonds in LiBH$_4$/Al$_2$O$_3$ and show that the conductivity in this composite is twice as high the one of LiBH$_4$/SiO$_2$ which could be explain by the fact that Al$_2$O$_3$ has higher density of OH surface groups than SiO$_2$ [81] and to a lesser extent by the difference in particle size (5 nm and 7 nm respectively) and surface area. Surface charge density has an important role in formation of B-O bonds and increased Li ion mobility and therefore surface engineering of oxides, to increase the surface charge density, should improve the conductivity of the LiBH$_4$ – oxide composites.

On the basis of analysis of scanning electron microscopy images (see Figure S10 in supplementary information), we have evaluated the size of the silica domains to be 0.5-1 µm, sizes much smaller than the initial particle sizes (19-37 µm), the size reduction occurring during ball milling. From simple geometrical considerations, the thickness of the conductive layer, taken as 10 % of the total volume of LiBH$_4$, is calculated to be of 2 to 4 nm. This is in agreement with the layer thickness calculated by Choi et al. [45] using the continuum percolation model developed by Roman.[82] In this model, which describes correctly the macroscopic transport properties, three phases are assumed: the insulating particles, the highly conductive interfacial layer and the "normally" conducting one, i.e unmodified LiBH$_4$. This macroscopic justification applies herein (**Figure 11**). For LiBH$_4$ nanoconfined in different mesoporous scaffold, of carbon or silica, a interfacial layer thicknesses of about 1 nm have been estimated [65,72] the thicker one being obtained for the silica based scaffolds.[66]
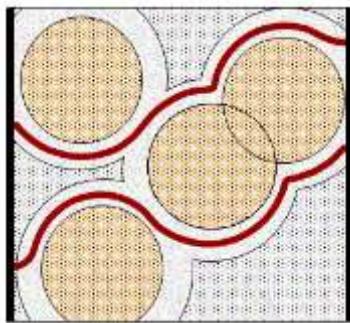
Figure 11. Macroscopic model for LiBH$_4$/SiO$_2$ conduction pathways. The spheres are SiO$_2$ particles surrounded by interfacial layers of high conductivity, embedded in porous LiBH$_4$ matrix. The red lines can represent Li+ paths. Adapted from Roman.[82]

Choi et al. obtained slightly higher conductivity for their composite electrolyte LiBH$_4$/SiO$_2$, using a different silica source, non-porous fumed silica vs porous aerogel, in this study. They measured the specific surface area, before milling, to be 362 m^2.g^{-1}, for 7 nm particles while for our purchased gel the surface area is given to be of 550 m^2.g^{-1} but including the inner surface area of the pores. The pore volume is given to be 0.8 cm^3.g^{-1} and of size 6 nm. Assuming spherical pores, we estimate the external surface area of silica gel to be of 150 m^2.g^{-1}. Thus, it is reasonable to assume that the fraction of interfacial LiBH$_4$, in contact with SiO$_2$ might be larger for fumed silica than for the gel and it results the observed conductivity difference. Here we assume that no or only a very small fraction of LiBH$_4$ is confined in the pores of the silica gel, this is confirmed by the DSC and X-ray diffraction measurements (Figure S8 and S9). If a fraction of LiBH$_4$ was nanoconfined one should observed a thermal event, corresponding the structural transition at lower temperature.[43] Therefore we can conclude that the dominant effect, leading to high conductivities does not result from the effect of nanoconfinement, like size reduction of the crystallites or resulting strain but originates from interaction of the ionic conductor with the insulating phase.

Again from simple geometrical consideration, assuming a number of surface hydroxyl group of 4 to 6 per nm^2,[83] we evaluate that up 10% of the LiBH$_4$, in the case of the 30/70 wt% composite, could for example react to form SiO-BH$_3$ as depicted in Eq. 6. This value is probably over estimated; it

assumes that the temperature during ball-milling is high enough and that all the surface groups get in contact with unreacted $LiBH_4$, however it indicates that the number of $SiO-BH_3$ is not negligible, as illustrated by the possible third intermediate boron population found in the NMR spectra and the QENS results obtained at low temperature (T<150K) where L1 or L2 would be attributed to BH_3 dynamics.

Charge-discharge cycling of solid-state Li-S batteries

Ten charge-discharge curves for a Li-S battery with 30/70 wt% LiBH4/SiO2 electrolyte are shown in **Figure 12** The discharge and charge plateaus show a slight slope unlike the flat plateaus found for Li-S cell with liquid electrolyte.[84] The batteries exhibit on average an overvoltage of about 0.15 V. As can be seen in **Figure 12.** the initial discharge is significantly longer than the following one and the cell exhibits a capacity of 3600 mAhg^{-1} which is more than double the theoretical capacity. During this initial discharge, two voltage plateaus can be observed: one at a higher voltage around 2.3 V and one at a lower voltage around 2.1 V. This observation is similar to the unexpected high capacity observed for the Li-S batteries based on thio-LISICON [6] or nanoconfined $LiBH_4$ [44] solid-electrolytes and Li-$Li_4Ti_5O_{12}$ batteries using LiBH4/LiI solid solution as electrolytes. [41] In case of the thio-LiSICON batteries, the high capacity was attributed to possible reactions of lithium with the carbon matrix of the positive electrode. During the second discharge, the cell reached a capacity of around 1500 mAh.g^{-1} of S which is 90% of the theoretical capacity. This is 100 time higher than the discharge capacity of the lithium titanate/$LiBH_4$ –LiI/Li cells proposed by Sveinbjörnsson, et al..[41] An average capacity loss of 7.2% was observed after each cycle and 35.8% of the capacity obtained during the second discharge was obtained during the fifth cycle. The insert in **Figure 12** shows an example of the evolution of the coulombic efficiency (CE) for a Li-S battery cycled at 0.03 C and 328K.
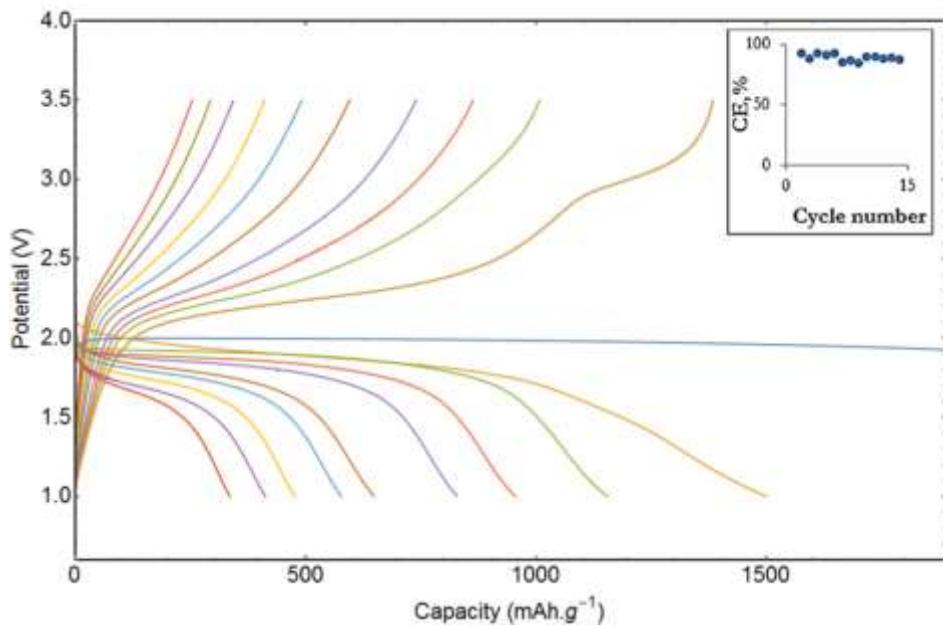
Figure 12. Discharge-charge cycles for a Li-S battery with 30/70 wt% $LiBH_4/SiO_2$ electrolyte at a rate 0.03 C and 328 K. The insert shows evolution of the coulombic efficiency (CE) with increasing cycle number

The high coulombic efficiency of 88.8% ± 2.7% (calculated average capacity loss) during the first 10 cycles proves the reversibility of the electrochemical reaction induced during the charge/discharge cycles and since the voltage plateaus are very close to the theoretical one (1675 mAhg^{-1} sulfur at 2.15 V) [4–10], we can exclude the existence of non-reversible electrochemical reaction (except for the first discharge). In fact, the fading capacity could be due to loss of contact as the electrolyte/electrode interface due to swelling of the positive electrode during cycling.

Impedance of solid state Li-S batteries

A Nyquist plot resulting from an Electrochemical Impedance Spectroscopy (EIS) measurement of a newly assembled Li-S cell is shown in Figure 13 (left). It is fitted with the equivalent circuit model: R_1-(R_2-CPE)-W (see Figure S11 in Supplementary information), where R_1 accounts for any internal resistances except those of the electrolyte taken into account by the R_2-CPE elements. The constant phase element (CPE) is used to model the capacitance within the electrolyte. The Warburg element

(W) models the finite-length diffusion of Li ions in the positive electrode.[41] The minima point in the

Nyquist plot gives the value of the overall cell resistivity (i.e. $R_c = R_1 + R_2$).
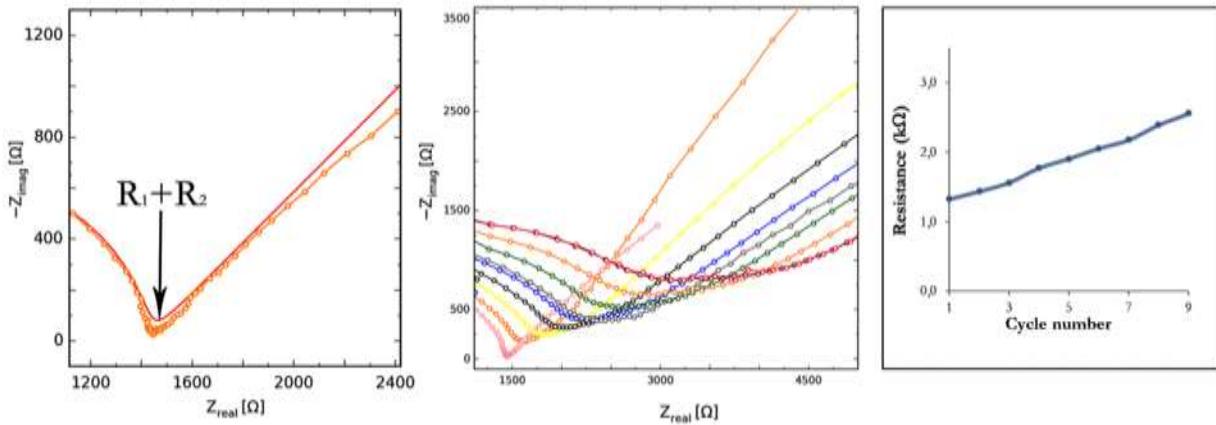
Figure 13. Left: Nyquist plot of EIS measurement of a newly assembled Li-S cell with 30/70 wt% $LiBH_4/SiO_2$ electrolyte. The measurement was performed before first discharge. Circles: experimental data, continuous line: fit. Middle: Nyquist plots of EIS measurements of a Li-S cell with 30/70 wt% $LiBH_4+SiO_2$ electrolyte. Right: Development of cell resistivity during cycling of a Li-S cell with 30/70 wt% $LiBH_4/SiO_2$ electrolyte.

The portion of arc in the high frequency region (left of the minima) is the typical contribution from

the electrolyte. It is possible that the arc consists of two or more overlapping components (bulk and

grain boundary Li^+ diffusion for example), [34] however they are not possible to separate with the

current setup. Figure 13 (middle) shows the Nyquist plot for EIS measurements performed on a Li-

S battery with 30/70 wt% $LiBH_4/SiO_2$ electrolyte acquired after each of discharge and Figure 13

(right) shows the evolution of the cell resistivity (Rc) with the cycles number read from Figure 13

(middle).

Rc for the freshly assembled cell was of 1.3 kΩ and upon cycling it increased to 1.45 kΩ after the

first cycle and to 2.8 kΩ after 10 cycles. Rc increases linearly (~+10%) with the number of cycles

therefore it is reasonable to assume that the electrochemical reaction taking place during the first

cycle and giving to the cell a capacity more than two times the theoretical one, does not lead to the

formation of a highly resistive Cathode Electrolyte Interface (CEI) as commonly observed in Li

batteries with liquid electrolytes and resulting in capacity loss during the first cycles. [85] Further

work is needed to explain the origin of the high capacity during the first discharge of a Li-S cell. The steadily increase of the cell resistivity could originate from the loss of contact between the solid electrolyte and the electrodes because of the mechanical stresses imposed to the different components. On the negative electrode side there is the stripping and plating of metallic lithium while on the cathode side the redox of S gives large volume changes (a 289 % increase in molar volume due to conversion of S to Li_2S).[6] The increase in the cell resistivity, however, does not lead to a large Ohmic drop through the cell, calculated to be of about 1 mV after the last cycle, and therefore cannot explain fully the fading capacity. The charge and discharge curves in **Figure 12** exhibit sloppy plateaus instead of the expected flat plateaus. The ends of the discharge have steeper slopes than the charge curves and the slopes are getting stepper and stepper with the cycle numbers. This can probably be explained by contact issues between the sulfur electrode and the composite electrolyte and by the more and more difficult access for lithium to react with sulfur. The increased slope toward the end of the discharge curves probably arises because it would be natural for Li^+ to first reacts with area where S is in good contact with the electrolyte and as the discharge proceeds, the sulfur reduction would take place in areas with ever less contact, resulting in an ever-greater overvoltage and consequently a steeper slope of the discharge curve. At the end, the fading capacity could be due to loss of contact at the electrolyte/electrode interface with less and less sulfur being available to react.

4. Conclusions

In this work we have investigated the origins of high Li^+ conductivity in solid-state electrolyte based on ball-milled $LiBH_4/SiO_2$ aerogel. QENS and NMR measurements show the presence of two different $LiBH_4$ fractions in the electrolyte, one exhibiting high lithium and hydrogen mobilities and which can account for high ionic conductivity of the electrolyte at room temperature. This modified

LiBH$_4$ exists despite the absence of nanoconfinement and might result from the interaction with the silica surface via the reaction with the silanol groups. To further increase the conductivity it is clear that one should aim at maximizing the contact area between LiBH$_4$ and SiO$_2$, i.e use silica of larger surface area and optimizing the ratio between the borohydride and silica. A second and complementary strategy will be to functionalize and structured the surface of the insulating material to increase the density and nature of the active surface groups.

The batteries have been cycled and show reasonable capacity retention (coulombic efficiency of 88.8% ± 2.7% and average capacity loss of 7.2% during the first 10 cycles). Further work is needed to explain the origin of the high capacity during the first discharge of a Li-S cell, however the presumably formed CEI layer does not seem to be a major limiting factor during second and onward cycles.

5. Supporting Information

Example of an EIS - Nyquist plot obtained at 333 K for 30/70 wt % LiBH$_4$/SiO$_2$ and its fit.

QENS Spectra at different temperatures (160, 200, 250K), for 30/70wt% LiBH$_4$/SiO$_2$, at Q=1.7239 Å^{-1} with a set energy transfer window of ±30μeV.

QENS spectra FWHM temperature dependency obtained from the fit of QENs Spectra for the two energy transfer window (±5 and ±30μeV) and at different temperatures.

Differential scanning calorimetry of 30/70wt% LiBH$_4$/SiO$_2$ and LiBH4.

X-ray powder diffraction pattern taken for 30/70wt% LiBH$_4$/SiO$_2$ and LiBH$_4$.

SEM image of the surface of a pressed 30/70% wt% LiBH$_4$/SiO$_2$ pellet

The equivalent circuit used for modelling impedance spectra of Li-S cells.

6. Acknowledgements

7. References

(1)   Manthiram, A.; Fu, Y.; Chung, S.; Zu, C.; Su, Y. Rechargeable Lithium - Sulfur Batteries. Chem. Rev. 2014, *114*, 11751–11787.

(2)   Bruce, P. G.; Freunberger, S. A.; Hardwick, L. J.; Tarascon, J.-M. Li–O$_2$ and Li–S Batteries with High Energy Storage. Nat. Mater. 2011, *11*, 172–172.

(3)   Younesi, R.; Veith, G. M.; Johansson, P.; Edstrom, K.; Vegge, T. Lithium Salts for Advanced Lithium Batteries: Li-Metal, Li-O$_2$, and Li-S. Energy Environ. Sci. 2015, *8*, 1905–1922.

(4)   Kim, J.; Lee, D. J.; Jung, H. G.; Sun, Y. K.; Hassoun, J.; Scrosati, B. An Advanced Lithium-Sulfur Battery. Adv. Funct. Mater. 2013, *23*, 1076–1080.

(5)   Song, M.-K.; Cairns, E. J.; Zhang, Y. Lithium/sulfur Batteries with High Specific Energy: Old Challenges and New Opportunities. Nanoscale 2013, *5*, 2186–2204.

(6)   Kobayashi, T.; Imade, Y.; Shishihara, D.; Homma, K.; Nagao, M.; Watanabe, R.; Yokoi, T.; Yamada, A.; Kanno, R.; Tatsumi, T. All Solid-State Battery with Sulfur Electrode and Thio-LISICON Electrolyte. J. Power Sources 2008, *182*, 621–625.

(7)   Manthiram, A.; Fu, Y.; Su, Y.-S. Challenges and Prospects of Lithium-Sulfur Batteries. Acc. Chem. Res. 2013, *46*, 1125–1134.

(8)   Lin, Z.; Liang, C. Lithium-Sulfur Batteries: From Liquid to Solid Cells. J. Mater. Chem. A 2015, *3*, 936–958.

(9)   Manthiram, A.; Chung, S.-H.; Zu, C. Lithium–Sulfur Batteries: Progress and Prospects. Adv. Mater. 2015, *27*, 1980–2006.

(10)   Kim, T. H.; Park, J. S.; Chang, S. K.; Choi, S.; Ryu, J. H.; Song, H. K. The Current Move of Lithium Ion Batteries towards the next Phase. Adv. Energy Mater. 2012, *2*, 860–872.

(11)   Nitta, N.; Wu, F.; Lee, J. T.; Yushin, G. Li-Ion Battery Materials: Present and Future. Mater. Today 2015, *18*, 252–264.

(12)   Zheng, S.; Han, P.; Han, Z.; Zhang, H.; Tang, Z.; Yang, J. High Performance C/S Composite Cathodes with Conventional Carbonate-Based Electrolytes in Li-S Battery. Sci. Rep. 2014, *4*, 4842.

(13)   Li, M.; Zhang, Y.; Wang, X.; Ahn, W.; Jiang, G.; Feng, K.; Lui, G.; Chen, Z. Gas Pickering Emulsion Templated Hollow Carbon for High Rate Performance Lithium Sulfur Batteries. Adv. Funct. Mater. 2016, 8408–8417.

(14)   Hoffmann, C.; Thieme, S.; Brückner, J.; Oschatz, M.; Biemelt, T.; Mondin, G.; Althues, H.; Kaskel, S. Nanocasting Hierarchical Carbide-Derived Carbons in Nanostructured Opal Assemblies for High-Performance Cathodes in Lithium-Sulfur Batteries. ACS Nano 2014, *8*, 12130–12140.

(15)   Yuan, Y.; Guihua, Y.; Judy J., C.; Hui, W.; Michael, V.; Yan, Y.; Zhenan, B.; Yi, C. Improving the Performance of Lithium-Sulfur Batteries by Conductive Polymer Coating. ACS Nano 2011, *5*, 9187–9193.

(16)   Xin, S.; Yin, Y. X.; Wan, L. J.; Guo, Y. G. Encapsulation of Sulfur in a Hollow Porous Carbon Substrate for Superior Li-S Batteries with Long Lifespan. Part. Part. Syst. Charact. 2013, *30*, 321–325.

(17)   Liu, X.; Shan, Z.; Zhu, K.; Du, J.; Tang, Q.; Tian, J. Sulfur Electrode Modified by Bifunctional Nafion/γ-Al_2O_3 Membrane for High Performance Lithium-Sulfur Batteries. J. Power Sources 2015, *274*, 85–93.

(18)   Hayashi, A.; Ohtomo, T.; Mizuno, F.; Tadanaga, K.; Tatsumisago, M. All-Solid-State Li/S Batteries with Highly Conductive Glass–ceramic Electrolytes. Electrochem. commun. 2003, *5*, 701–705.

(19)   Jeon, B. H.; Yeon, J. H.; Kim, K. M.; Chung, I. J. Preparation and Electrochemical Properties of Lithium-Sulfur Polymer Batteries. J. Power Sources 2002, *109*, 89–97.

(20)   Yu, X.; Xie, J.; Yang, J.; Wang, K. All Solid-State Rechargeable Lithium Cells Based on Nano-Sulfur Composite Cathodes. J. Power Sources 2004, *132*, 181–186.

(21)   Hayashi, A.; Ohtomo, T.; Mizuno, F.; Tadanaga, K.; Tatsumisago, M. Rechargeable Lithium Batteries, Using Sulfur-Based Cathode Materials and Li2S–P2S5 Glass-Ceramic Electrolytes. Electrochim. Acta 2004, *50*, 893–897.

(22)   Belous, A. G.; Novitskaya, G. N.; Polyanetskaya, S. V.; Gornikov, Y. I. Study of Complex Oxides with the Composition $LA_{2/3-X}LI_{3X}TIO_3$. Inorg. Mater. 1987, *23*, 412–415.

(23)   Inaguma, Y.; Liquan, C.; Itoh, M. High Ionic Conductivity in Lithium Lanthanum Titanate. Solid State Commun. 1993, *86*, 689–693.

(24)   Seo, I.; Martin, S. W. New Developments in Solid Electrolytes for Thin-Film Lithium Batteries. Lithium Ion Batter. New Dev. 2012, *1*, 101–144.

(25)   Bruce, P. G.; West, A. R. The A-C Conductivity of Polycrystalline LISICON, $Li_{2+2x}Zn_{1-X}GeO_4$, and a Model for Intergranular Constriction Resistances. J. Electrochem. Soc. 1983, *130*, 662–669.

(26)   Kamaya, N.; Homma, K.; Yamakawa, Y.; Hirayama, M.; Kanno, R.; Yonemura, M.; Kamiyama, T.; Kato, Y.; Hama, S.; Kawamoto, K.; et al. A Lithium Superionic Conductor. Nat. Mater. 2011, *10*, 682–686.

(27)   Bachman, J. C.; Muy, S.; Grimaud, A.; Chang, H. H.; Pour, N.; Lux, S. F.; Paschos, O.; Maglia, F.; Lupart, S.; Lamp, P.; et al. Inorganic Solid-State Electrolytes for Lithium Batteries: Mechanisms and Properties Governing Ion Conduction. Chem. Rev. 2016, *116*, 140–162.

(28)   Unemoto, A.; Matsuo, M.; Orimo, S. Complex Hydrides for Electrochemical Energy Storage. Adv. Funct. Mater. 2014, *24*, 2267–2279.

(29)   de Jongh, P. E.; Blanchard, D.; Matsuo, M.; Udovic, T. J.; Orimo, S. Complex Hydrides as Room-Temperature Solid Electrolytes for Rechargeable Batteries. Appl. Phys. A 2016, *122*, 251.

(30)   Züttel, A.; Wenger, P.; Rentsch, S.; Sudan, P.; Mauron, P.; Emmenegger, C. $LiBH_4$ a New Hydrogen Storage Material. al., J. Power Sources, *118*, 1, 2003.

(31)   Lodziana, Z.; Vegge, T. Structural Stability of Complex Hydrides: LiBH4 Revisited. Phys. Rev. Lett. 2004, *93*, 145501.

(32)   Blanchard, D.; Shi, Q.; Boothroyd, C. B.; Vegge, T. Reversibility of Al/Ti Modified $LiBH_4$. J. Phys. Chem. C 2009, *113*, 14059–14066.

(33)   Matsuo, M.; Nakamori, Y.; Orimo, S.; Maekawa, H.; Takamura, H. Lithium Superionic Conduction in Lithium Borohydride Accompanied by Structural Transition. Appl. Phys. Lett. 2007, *91*, 224103.

(34)   Sveinbjörnsson, D.; Myrdal, J. S. G.; Blanchard, D.; Bentzen, J. J.; Hirata, T.; Mogensen, M. B.; Norby, P.; Orimo, S.-I.; Vegge, T. Effect of Heat Treatment on the Lithium Ion Conduction of the $LiBH_4$-LiI Solid Solution. J. Phys. Chem. C 2013, *117*, 3249–3257.

(35)   Epp, V.; Wilkening, M. Fast Li Diffusion in Crystalline $LiBH_4$ due to Reduced Dimensionality: Frequency-Dependent NMR Spectroscopy. Phys. Rev. B 2010, *82*, 20301.

(36)   Mohtadi, R.; Orimo, S. The Renaissance of Hydrides as Energy. Nat. Publ. Gr. 2016, *2*, 1–16.

(37)   Unemoto, A.; Yasaku, S.; Nogami, G.; Tazawa, M.; Taniguchi, M.; Matsuo, M.; Ikeshoji, T.; Orimo, S. Development of Bulk-Type All-Solid-State Lithium-Sulfur Battery Using $LiBH_4$ Electrolyte. Appl. Phys. Lett. 2014, *105*, 83901.

(38)   Aeberhard, P.C., Refson, K.; David, W. I. F. Molecular Dynamics Investigation of the Disordered Crystal Structure of Hexagonal $LiBH_4$. Phys. Chem. Chem. Phys. 2013, *15*, 8081–8087.

(39)   Maekawa, H.; Matsuo, M.; Takamura, H.; Ando, M.; Noda, Y.; Karahashi, T.; Orimo, S. Halide-Stabilized $LiBH_4$, a Room-Temperature Lithium Fast-Ion Conductor. J. Am. Chem. Soc. 2009, *131*, 894–895.

(40)   Oguchi, H.; Matsuo, M.; Hummelshøj, J. S.; Vegge, T.; Nørskov, J. K.; Sato, T.; Miura, Y.; Takamura, H.; Maekawa, H.; Orimo, S. Experimental and Computational Studies on Structural Transitions in the $LiBH_4$-LiI Pseudobinary System. Appl. Phys. Lett. 2009, *94*, 141912.

(41)   Sveinbjörnsson, D.; Christiansen, A. S.; Viskinde, R.; Norby, P.; Vegge, T. The $LiBH_4$-LiI Solid Solution as an Electrolyte in an All-Solid-State Battery. J. Electrochem. Soc. 2014, *161*, A1432–A1439.

(42)   Unemoto, A.; Chen, C.; Wang, Z.; Matsuo, M.; Ikeshoji, T.; Orimo, S. Pseudo-Binary Electrolyte, $LiBH_4$ –LiCl, for Bulk-Type All-Solid-State Lithium-Sulfur Battery. Nanotechnology 2015, *26*, 254001.

(43)   Blanchard, D.; Nale, A.; Sveinbjörnsson, D.; Eggenhuisen, T. M.; Verkuijlen, M. H. W.; Suwarno; Vegge, T.; Kentgens, A. P. M.; De Jongh, P. E. Nanoconfined LiBH4 as a Fast Lithium Ion Conductor. Adv. Funct. Mater. 2015, *25*, 184–192.

(44)   Das, S.; Ngene, P.; Norby, P.; Vegge, T.; Jongh, P. E. De; Blanchard, D. All-Solid-State Lithium-Sulfur Battery Based on a Nanoconfined $LiBH_4$ Electrolyte. J. Electrochem. Soc. 2016, *163*, 2029–2034.

(45)   Choi, Y. S.; Lee, Y.-S.; Oh, K. H.; Cho, Y. W. Interface-Enhanced Li Ion Conduction in a $LiBH_4$ –SiO_2 Solid Electrolyte. Phys. Chem. Chem. Phys. 2016, *18*, 22540–22547.

(46)   Choi, Y. S.; Lee, Y.-S.; Choi, D.-J.; Chae, K. H.; Oh, K. H.; Cho, Y. W. Enhanced Li Ion Conductivity in $LiBH_4$ –Al_2O_3 Mixture via Interface Engineering. J. Phys. Chem. C 2017, *121*, 26209–26215.

(47)   Robin Bendall, M.; Gordon, R. E. Depth and Refocusing Pulses Designed for Multipulse NMR with Surface Coils. J. Magn. Reson. 1983, *53*, 365–385.

(48)   Bielecki, A.; Burum, D. P. Temperature Dependence of ^{207}Pb MAS Spectra of Solid Lead Nitrate. An Accurate, Sensitive Thermometer for Variable-Temperature MAS. J. Magn. Reson. Ser. A 1995, *116*, 215–220.

(49)   Azuah, R. T.; Kneller, L. R.; Qiu, Y.; Brown, C. M.; Copley, J. R. D.; Dimeo, R. M. DAVE?: A Comprehensive Software Suite. J. Res. Natl. Inst. Stand. Technol. 2009, *114*, 341–358.

(50)   Beekmans, N. M.; Heyne, L. Correlation between Impedance, Microstructure and Composition of Calcia-Stabilized Zirconia. Electrochim. Acta 1976, *21*, 303–310.

(51)   Haile, S. M.; West, D. L.; Campbell, J. The Role of Microstructure and Processing on the Proton Conducting Properties of Gadolinium-Doped Barium Cerate. J. Mater. Res. 1998, *13*, 1576–1595.

(52)   Remhof, A.; Züttel, A.; Ramirez-Cuesta, T.; García-Sakai, V.; Frick, B. Hydrogen Dynamics in the Low Temperature Phase of $LiBH_4$ Probed by Quasielastic Neutron Scattering. Chem. Phys. 2013, *427*, 18–21.

(53)   Skripov, A. V.; Soloninin, A. V.; Filinchuk, Y.; Chernyshov, D. Nuclear Magnetic Resonance Study of the Rotational Motion and the Phase Transition in LiBH4. J. Phys. Chem. C 2008, *112*, 18701–18705.

(54)   Buchter, F.; Lodziana, Z.; Mauron, P.; Remhof, a.; Friedrichs, O.; Borgschulte, a.; Züttel, a.; Sheptyakov, D.; Strässle, T.; Ramirez-Cuesta, a. Dynamical Properties and Temperature Induced Molecular Disordering of $LiBH_4$ and $LiBD_4$. Phys. Rev. B 2008, *78*, 1–9.

(55)   Soloninin, A. V.; Skripov, A. V.; Buzlukov, A. L.; Stepanov, A. P. Nuclear Magnetic Resonance Study of Li and H Diffusion in the High-Temperature Solid Phase of $LiBH_4$. J. Solid State Chem. 2009, *182*, 2357–2361.

(56)   Blanchard, D.; Riktor, M. D.; Maronsson, J. B.; Jacobsen, H. S.; Kehres, J.; Sveinbjo, D.; Bardaji, E. G.; Le, A.; Juranyi, F.; Wuttke, J.; et al. Hydrogen Rotational and Translational Diffusion in Calcium Borohydride from Quasielastic Neutron Scattering and DFT Calculations. Jounal Phys. Chemitry C 2010, *114*, 20249–20257.

(57)   Remhof, A.; Lodziana, Z.; Martelli, P.; Friedrichs, O.; Züttel, A.; Skripov, A.; Embs, J.; Strässle, T. Rotational Motion of BH_4 Units in MBH4 (M=Li,Na,K) from Quasielastic Neutron Scattering and Density Functional Calculations. Phys. Rev. B 2010, *81*, 1–9.

(58)   Martelli, P.; Remhof, A.; Borgschulte, A.; Ackermann, R.; Strässle, T.; Embs, J. P.; Ernst, M.; Matsuo, M.; Orimo, S.-I.; Züttel, A. Rotational Motion in $LiBH_4$/LiI Solid Solutions. J. Phys. Chem. A 2011, *115*, 5329–5334.

(59)   Jimura, K.; Hayashi, S. Reorientational Motion of BH_4 Ions in Alkali Borohydrides MBH_4 (M = Li, Na, K) as Studied by Solid-State NMR. J. Phys. Chem. C 2012, *116*, 4883–4891.

(60)   Blanchard, D.; Maronsson, J. B.; Riktor, M. D.; Kehres, J.; Sveinbjörnsson, D.; Bardají, E. G.; Léon, A.; Juranyi, F.; Wuttke, J.; Lefmann, K.; et al. Hindered Rotational Energy

Barriers of BH_4^- Tetrahedra in Beta-$Mg(BH_4)_2$ from Quasielastic Neutron Scattering and DFT Calculations. J. Phys. Chem. C 2012, *116*, 2013.

(61)   Verdal, N.; Udovic, T. J.; Rush, J. J.; Wu, H.; Skripov, A. V. Evolution of the Reorientational Motions of the Tetrahydroborate Anions in Hexagonal $LiBH_4$-LiI Solid Solution by High-Q Quasielastic Neutron Scattering. J. Phys. Chem. C 2013, *117*, 12010–12018.

(62)   Udovic, T. J.; Verdal, N.; Rush, J. J.; De Vries, D. J.; Hartman, M. R.; Vajo, J. J.; Gross, A. F.; Skripov, A. V. Mapping Trends in the Reorientational Mobilities of Tetrahydroborate Anions via Neutron-Scattering Fixed-Window Scans. J. Alloys Compd. 2013, *580*, S47–S50.

(63)   Remhof, A.; Yan, Y.; Embs, J. P.; Sakai, V. G.; Nale, A.; De Jongh, P. E.; Lodziana, Z.; Züttel, A. Rotational Disorder in Lithium Borohydride. EPJ Web Conf. 2015, *83*, 2014.

(64)   Remhof, A.; Mauron, P.; Züttel, A.; Embs, J. P.; Lodziana, Z.; Ramirez-Cuesta, A. J.; Ngene, P.; De Jongh, P. Hydrogen Dynamics in Nanoconfined Lithiumborohydride. J. Phys. Chem. C 2013, *117*, 3789–3798.

(65)   Verdal, N.; Udovic, T. J.; Rush, J. J.; Liu, X.; Majzoub, E. H.; Vajo, J. J.; Gross, A. F. Dynamical Perturbations of Tetrahydroborate Anions in $LiBH_4$ due to Nanoconfinement in Controlled-Pore Carbon Scaffolds. J. Phys. Chem. C 2013, *117*, 17983.

(66)   Suwarno; Ngene, P.; Nale, A.; Eggenhuisen, T. M.; Oschatz, M.; Embs, J. P.; Remhof, A.; De Jongh, P. E. Confinement Effects for Lithium Borohydride: Comparing Silica and Carbon Scaffolds. J. Phys. Chem. C 2017, *121*, 4197–4205.

(67)   Tsang, T.; Farrar, T. C. Nuclear Magnetic Relaxation Studies of Internal Rotations and Phase Transitions in Borohydrides of Lithium, Sodium, and Potassium. J. Chem. Phys. 1969, *50*, 3498–3502.

(68)   Frick, B.; Combet, J.; Van Eijck, L. New Possibilities with Inelastic Fixed Window Scans and Linear Motor Doppler Drives on High Resolution Neutron Backscattering Spectrometers.

Nucl. Instruments Methods Phys. Res. Sect. A Accel. Spectrometers, Detect. Assoc. Equip. 2012, *669*, 7–13.

(69)   Bée, M. Quasielastic Neutron Scattering; Hilger, A., Ed.; Bristol and Philadelphia, PA, 1988.

(70)   Filinchuk, Y.; Chernyshov, D.; Cerny, R. Lightest Borohydride Probed by Synchrotron X-Ray Diffraction?: Experiment Calls for a New Theoretical Revision. Jounal Phys. Chemitry C 2008, *112*, 10579–10584.

(71)   Verkuijlen, M. H. W.; Ngene, P.; De Kort, D. W.; Barré, C.; Nale, A.; Van Eck, E. R. H.; Van Bentum, P. J. M.; De Jongh, P. E.; Kentgens, A. P. M. Nanoconfined $LiBH_4$ and Enhanced Mobility of Li^+ and BH_4^- Studied by Solid-State NMR. J. Phys. Chem. C 2012, *116*, 22169–22178.

(72)   Shane, D. T.; Corey, R. L.; McIntosh, C.; Rayhel, L. H.; Bowman, R. C.; Vajo, J. J.; Gross, A. F.; Conradi, M. S. $LiBH_4$ in Carbon Aerogel Nanoscaffolds: An NMR Study of Atomic Motions. J. Phys. Chem. C 2010, *114*, 4008–4014.

(73)   Hwang, S.; Lee, H.; To, M.; Lee, Y.; Whan, Y.; Choi, H.; Kim, C. Probing Molecular Dynamics of Metal Borohydrides on the Surface of Mesoporous Scaffolds by Multinuclear High Resolution Solid State NMR. J. Alloys Compd. 2015, *645*, S316–S319.

(74)   Shane, D. T.; Bowman, R. C.; Conradi, M. S. Exchange of Hydrogen Atoms Between BH_4 in $LiBH_4$. J. Phys. Chem. C 2009, *113*, 5039–5042.

(75)   Shane, D. NMR Study of Borohydrides for Hydrogen Storage Applications. All Theses Diss. 2011, 320.

(76)   Senadheera, L.; Carl, E. M.; Ivancic, T. M.; Conradi, M. S.; Bowman, R. C.; Hwang, S. J.; Udovic, T. J. Molecular H_2 Trapped in AlH_3 Solid. J. Alloys Compd. 2008, *463*, 1–5.

(77)   Sorte, E. G.; Bowman, R. C.; Majzoub, E. H.; Verkuijlen, M. H. W.; Udovic, T. J.; Conradi, M. S. Mobile Species in $NaAlH_4$. J. Phys. Chem. C 2013, *117*, 8105–8113.

(78)   Unemoto, A.; Wu, H.; Udovic, T. J.; Matsuo, M.; Ikeshoji, T.; Orimo, S. Fast Lithium-Ionic Conduction in a New Complex Hydride–sulphide Crystalline Phase. Chem. Commun. 2016, *52*, 564–566.

(79)   Liang, C. C. Conduction Characteristics of the Lithium Iodide-Aluminum Oxide Solid Electrolytes. J. Electrochem. Soc. 1973, *120*, 1289.

(80)   Myrdal, J. S. G.; Blanchard, D.; Sveinbjörnsson, D.; Vegge, T. Li-Ion Conduction in the $LiBH_4$:LiI System from Density Functional Theory Calculations and Quasi-Elastic Neutron Scattering. J. Phys. Chem. C 2013, *117*, 9084–9091.

(81)   Gunko, V. M.; Turov, V. V; Chuiko, A. A. Fundamentals of Nanosilica Applications for Human Protection. In Surface Chemistry in Biomedical and Environmental Science.; Blitz J.P., G. V. M., Ed.; Springer: Dordrecht, 2006; 177–190.

(82)   Roman, H. E. A Continuum Percolation Model for Dispersed Ionic Conductors. J. Phys. Condens. Matter 1990, *2*, 3909–3917.

(83)   Binder, A.; Heel, A.; Kasper, G. Deposition of Palladium Nanodots of Controlled Size and Density onto Surface-Modified SiO_2 Particles by an Atmospheric Pressure CVS/MOCVD Process. Chem. Vap. Depos. 2007, *13*, 48–54.

(84)   Ji, X.; Lee, K. T.; Nazar, L. F. A Highly Ordered Nanostructured Carbon-Sulphur Cathode for Lithium-Sulphur Batteries. Nat. Mater. 2009, *8*, 500–506.

(85)   Verma, P.; Maire, P.; Novák, P. A Review of the Features and Analyses of the Solid Electrolyte Interphase in Li-Ion Batteries. Electrochim. Acta 2010, *55*, 6332–6341.

Table of Graphic